Lawrence Berkeley National Laboratory

Title

Minute-MOFs: Ultrafast Synthesis of M2(dobpdc) Metal–Organic Frameworks from Divalent Metal Oxide Colloidal Nanocrystals

Permalink

https://escholarship.org/uc/item/39n8d614

Authors

Maserati, Lorenzo
Meckler, Stephen M
Li, Changyi
et al.

Minute-MOFs: Ultrafast Synthesis of M$_2$(dobpdc) Metal–Organic Frameworks from Divalent Metal Oxide Colloidal Nanocrystals

Lorenzo Maserati,[†] Stephen M. Meckler,[†,‡] Changyi Li,[†,§] and Brett A. Helms*[,†]

[†]The Molecular Foundry, Lawrence Berkeley National Laboratory, One Cyclotron Road, Berkeley, California 94720, United States
[‡]Department of Chemistry and [§]Department of Chemical and Biomolecular Engineering, University of California, Berkeley, California 94720, United States

Ⓢ *Supporting Information*

ABSTRACT: The material demands for metal–organic frameworks (MOFs) for next-generation energy-efficient CO$_2$ capture technologies necessitate advances in their expedient and scalable synthesis. Toward that end, the recently discovered expanded MOF-74, or M$_2$(dobpdc), where M = divalent metal cation and dobpdc = 4,4′-dioxido-3,3′-biphenyldicarboxylate, can now be prepared in minutes via a controlled dissolution–crystallization route from divalent metal oxides as precursors. We show that the available surface area of the metal oxide plays a critical role in the precursor dissolution, which was found to be rate-limiting. Based on this understanding of the reaction trajectory, we pushed the chemical transformation to its fringe kinetic limit by configuring the metal oxide precursors as ligand-free colloidal metal oxide nanocrystals, which allowed MOF formation in less than 1 min. MOFs prepared by this strategy were highly crystalline, with BET surface areas on par with conventional multihour syntheses from metal halide salts. This method was also applied successfully in the synthesis of M$_2$(dobdc) MOFs, highlighting its generality. Our work challenges the conventional wisdom that plurality of steps in MOF formation is inherently time-intensive.
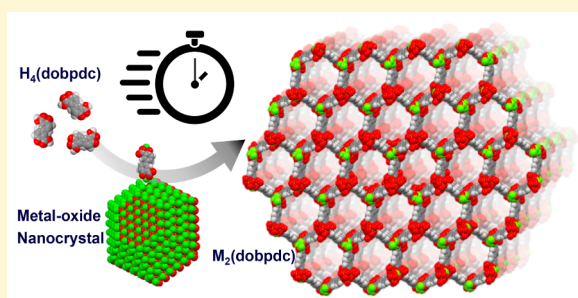
INTRODUCTION

Metal–organic frameworks (MOFs) are microporous crystalline solids constructed from metal ions or clusters covalently linked by organic ligands.[1,2] The tunability of their composition, architecture, and properties has advanced the fields of drug delivery,[3,4] catalysis,[5–7] sensors,[8–10] optoelectronics,[11–17] electrochemistry,[18–22] gas separations,[23–30] and gas storage.[31–33] During MOF crystallization, molecular precursors chemically transform into active monomers that crystallize into reticular architectures through a nucleation and growth process, in some cases requiring the formation of metal-oxo clusters from several metal ions and an endogenous source of oxygen.[34,35] While the mechanistic underpinnings of these transformations are still under investigation,[36,37] kinetic factors involving reaction byproducts may ultimately limit the rate of MOF formation from molecular precursors.

Here we report an exceptionally rapid synthesis of high quality M$_2$(dobpdc) MOFs (dobpdc = 4,4′-dioxido-3,3′-biphenyldicarboxylate), i.e., the expanded M-MOF-74 series, that substitutes conventional divalent metal salts with divalent metal oxides: MO = MgO, MnO, CoO, NiO, or ZnO. This (pseudo)halide-free route avoids the generation of acidic byproducts otherwise inherent to conventional M$_2$(dobpdc) syntheses; as a result, the reaction time needed decreases significantly,[38] in some cases, by several orders of magnitude (Figure 1). We investigated in detail the reaction pathway using ex situ X-ray diffraction (XRD) and scanning electron microscopy (SEM), which indicated that M$_2$(dobpdc) formation proceeded via a dissolution–crystallization mechanism. Through our analysis of MO precursor morphology, surface area, and composition-dependent etch rate, we determined that MO dissolution is rate-limiting. Notably, then, scaling the dimensions of the MO precursor to nanoscopic dimensions allows these MOFs to be prepared in high quality in mere minutes without residual MO. As ultimate demonstrations of the unprecedented opportunities for rate-acceleration, we synthesized Zn$_2$(dobpdc) MOFs from 7 nm ligand-stripped[39] ZnO colloidal nanocrystals (NCs) in less than 1 min and Co$_2$(dobpdc) MOFs from 9 nm ligand-stripped CoO[40] colloidal nanocrystals in less than 5 min. While metal oxides have been used as precursors for a select group of MOFs, in particular ZnO,[41–46] to the best of our knowledge, this is the first synthesis of M$_2$(dobpdc) using them; moreover, ours is the most rapid M$_2$(dobpdc) synthesis from any starting material (Scheme 1). Colloidal divalent MO nanocrystals are unexpectedly privileged in that regard.
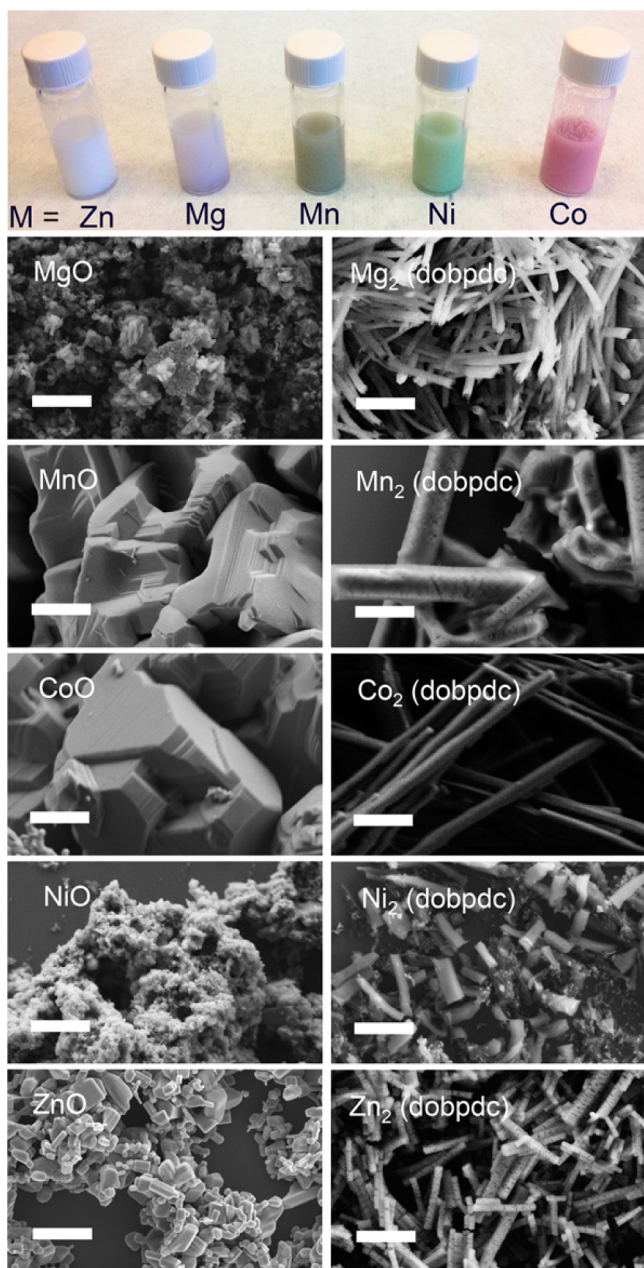
RESULTS AND DISCUSSION

M$_2$(dobpdc) MOFs and their diamine-modified derivatives have shown exceptional promise as next-generation materials

Figure 1. Top: Photograph of the M_2(dobpdc) MOFs dispersed in methanol. Bottom: scanning electron micrographs of MO precursors (left column) and their respective reaction products after high-temperature treatment with H_4(dobpdc) in DMF. Scale bars are 1.0 μm.

for energy-efficient CO_2 capture.[27,47−49] For diamine-modified M_2(dobpdc) MOFs, CO_2 adsorption involves the insertion of CO_2 into metal-amine bonds, which initiates rapid reorganization of the diamines into ordered chains of ammonium carbamates along the open channels.[48,50−52] The thermodynamics governing CO_2 uptake in these sorbents change dramatically with swings in either pressure or temperature; the sensitivity to those swings depends on the metal and the diamine. As a result, this scheme for CO_2 adsorption/desorption heralds an alternative, low-cost approach to CO_2 scrubbing in power plants.[53] Methods allowing their scalable and expedient production would significantly improve their

Scheme 1. Minute-MOF Concept and Realization[a]
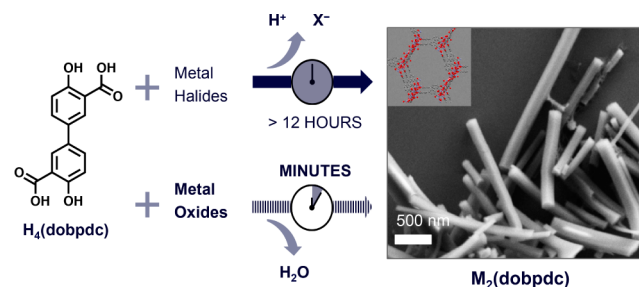
[a]MOFs, such as M_2(dobpdc), are generated in minutes under controlled reaction conditions from divalent metal oxides as precursors. Conventional syntheses from metal (pseudo)halide salts generate acidic byproducts and require multi-hour reaction times. Scale bar is 500 μm.

prospects in this regard and, in the short term, aid in their validation in pilot-scale prototypes.

One of the factors currently limiting their expedient production is that reaction times in excess of 12 h are required when preparing M_2(dobpdc) in solution (e.g., N,N-diethylformamide) from metal halide or metal pseudohalide salts and H_4(dobpdc) ligand. We hypothesized that the generation of acidic byproducts during this sequence of reactions may contribute to slow reaction times for this MOF. Recent studies have concluded as much in the synthesis of porous flexible iron fumarate MIL-88A MOF when acids were present. Organic acids were shown to inhibit crystallization while also contributing to a lower yield and a smaller particle size; conversely, increasing the pH had the opposite effect.[38] Were it possible to avoid acidic byproducts, e.g., via dissolution of MO solids as precursors, then the integration of H_4(dobpdc) into M_2(dobpdc) MOFs could, in principle, proceed at a faster rate.

Our optimized (pseudo)halide-free M_2(dobpdc) synthesis involves the temperature-assisted dissolution of H_4(dobpdc) in N,N-dimethylformamide at 120 °C, where $[H_4(dobpdc)]_0 = 0.50$ M, and subsequent addition of the MO solid. The reaction was allowed to proceed until the solid-to-solid transformation was complete (minutes to hours, depending on the MO). Several of the reactions generated highly colored products, which was most evident after cleanup (Figure 1).

In navigating the reaction space for this chemical transformation, we noted that the composition and morphology of the MO precursor played central roles in the rate of M_2(dobpdc) formation (Figure 1). The most rapid transformations were observed using MgO and ZnO solids as precursors to Mg_2(dobpdc) and Zn_2(dobpdc), respectively, with yields of 67% isolated yield for Mg_2(dobpdc) and 88% isolated yield for Zn_2(dobpdc). Interestingly, these reaction conditions were also applied successfully in the synthesis of standard M-MOF-74 materials, M_2(dobdc), when 2,5-dihydroxy-1,4-benzenedicarboxylic acid, H_4(dobdc), was used in the transformation. Whereas for M = Co, Fe, Ni, pure phase of M_2(dobdc) materials were obtained, chemical transformations employing ZnO solids led to mixed-phase materials (Figure S1).

Crystallinity and Porosimetry as Quality Metrics. Despite their unconventional method of preparation, the M_2(dobpdc) MOFs generated were of excellent quality as evidenced by their high crystallinity (Figure 2a−c, Figure S2), high surface areas (Figure 2c,d), and TGA analysis (Figure S3).
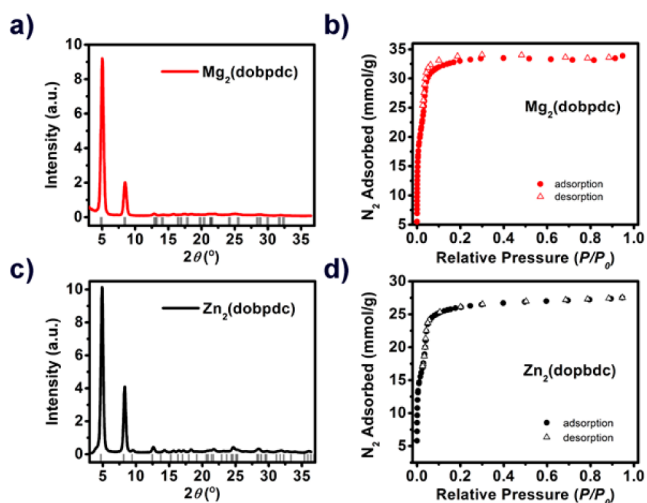
Figure 2. (a,b) XRD patterns and (c,d) BET surface area measurements for the Mg_2(dobpdc) (red curves) and Zn_2(dobpdc) (black curves).

Figure 3. SEM along the reaction trajectory of MgO to Mg_2(dobpdc): (a) 30 s; (b) 1 min; (c) 2 min; (d) 5 min; (e) 10 min; (f) 60 min. Scale bars for all panels are 2.0 μm; the inset scale bar is 500 nm.

All XRD spectra were well matched to their expected and previously reported data. Furthermore, their BET surface areas, 2290 ± 30 m^2 g^{-1} for Zn_2(dobpdc) and 2910 ± 40 m^2 g^{-1} for Mg_2(dobpdc), were in line with previous reports[47,48] (Table S1); the lack of hysteresis in the adsorption/desorption curves further indicated excellent measurement reliability and the absence of micropore blockages or other structure-related mass-transport bottlenecks. Finally, to demonstrate that Mg_2(dobpdc) MOFs exhibit characteristic CO_2-adsorption properties as previously reported,[47,48] we loaded N,N'-dimethylethylenediamine (mmen) into the framework, where they are chemisorbed at the open metal centers in the framework; indeed, we observed the expected step-function in CO_2 uptake at low pressure (Figure S4).

Assessment of the Reaction Trajectory from MO Dissolution to M$_2$(dobpdc) Crystallization. In contrast to previously reported metal oxide-to-MOF chemical transformations,[43,44] we did not observe significant pseudomorphic replication or self-limited growth of the MOF around the MO starting materials (Figure 1). To understand this outcome better, we monitored in greater detail the dissolution–crystallization trajectory of MgO to Mg_2(dobpdc) at different reaction times by sampling aliquots and analyzing the intermediates using ex situ SEM (Figure 3). Within the first 30 s of the transformation, we found that clusters of Mg_2(dobpdc) had sprouted from common nucleation points across the MgO surface (Figures 3a,b). After 2 min, these growths elongated (Figure 3c), and after 5 min, urchin-like morphologies were prevalent (Figure 3d). At this stage of the reaction, the XRD pattern matched that for Mg_2(dobpdc) with a small peak at 44° attributed to unreacted MgO (Figure S5a). After 10 min, the characteristic, highly anisotropic M_2(dobpdc) rod morphology (Figure 3e) was distinguishable from the faster forming clusters, and the MgO signature in the XRD was no longer present (Figure S5b). The crystal shape and crystallinity did not change significantly as reaction times were increased further, e.g., after 60 min (Figures 3f and S5b). The presence of MgO while M_2(dobpdc) rods are forming suggests MO etching is the rate-limiting step, signifying M^{2+} availability as a critical factor in optimizing this reaction pathway.
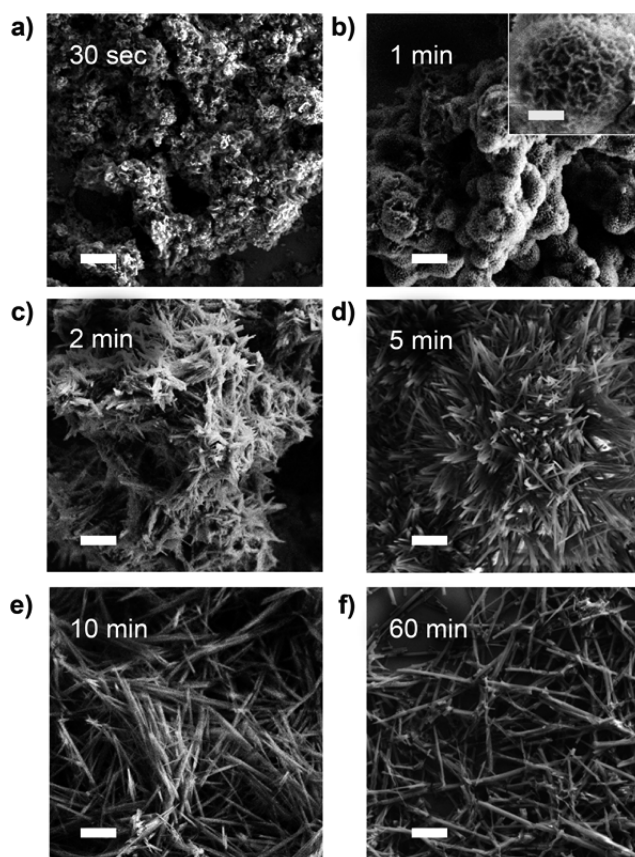
We found that the kinetic trajectories of MOF formation from ZnO and CoO were strikingly similar to that for MgO. However, the reaction was considerably slower in both cases: Zn_2(dobpdc) appeared 10 min after the reaction was initiated, and its crystallinity improved significantly between 30−60 min (Figure S6); however, CoO required at least 2 h to dissolve and begin to crystallize as Co_2(dobpdc) (Figure S7).

MO Etching Kinetics. In order to quantify the precursor dissolution rate underpinning the availability of M^{2+} during MOF formation, we introduced MO solids to a solution of salicylic acid (H_2(sal)) in DMF at 120 °C (i.e., our optimized reaction conditions). Salicylic acid here serves as a monofunctional analogue to H_4(dobpdc), which allowed us to track MO dissolution without contributing influence from other chemical species also involved in MOF crystallization. The time-evolution of MO etching by salicylic acid was observed using in situ Fourier transform infrared spectroscopy (FT-IR). Spectra were collected every 15 s over a spectral range of 600 to 2000 cm^{-1} (Figure S8). Metal salicylate formation $M[H(sal)]_2$ coincided with the disappearance of the H_2(sal) C−O stretch at 1219 cm^{-1}. This phenomenon was observed in all samples analyzed and was therefore a useful and selective marker for MO dissolution. Figure 4 shows the IR spectral changes over time from 1180 to 1300 cm^{-1} and the decrease in signal intensity, evidenced in the 2-D plot as a transition from red to blue, at 1219 cm^{-1} during the etching of ZnO, MgO, and CoO.

Our investigation of the etching process by ex situ SEM had indicated that salicylic acid first etches channels on the surface
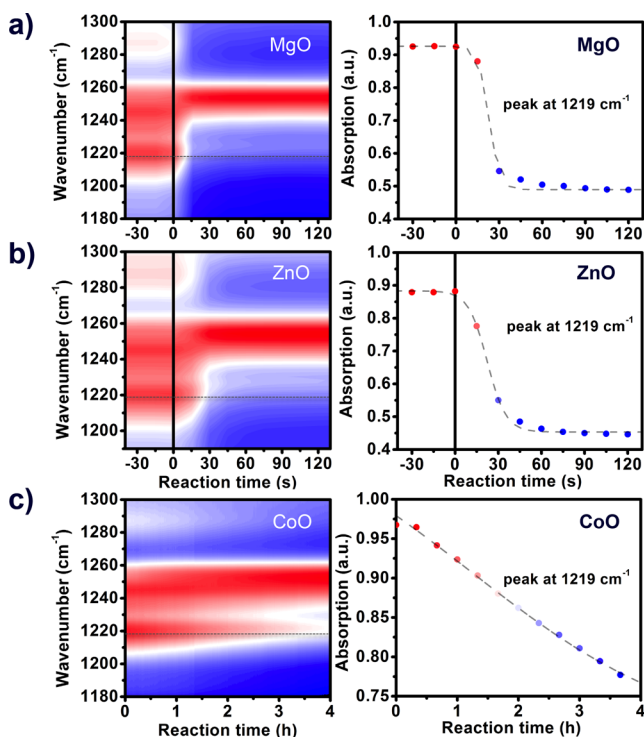
Figure 4. In situ FT-IR spectra was used to quantify the etch rates of divalent metal oxides in the presence of salicylic acid, $H_2(sal)$. Solid MO precursors were added to solution of $H_2(sal)$ in DMF (2.0 M) at 120 °C, and the spectra were recorded in situ at 15 s intervals. IR spectra over an energy range of 1180−1300 cm^{-1} are plotted versus reaction time. The color scale is set to distinguish high absorption (red) from low absorption (blue). Data along the indicated line-cuts at 1219 cm^{-1} represent the time-evolution of the interconversion of $H_2(sal)$ to $M[H(sal)]_2$ (right column). These data were fit using the Prout−Tompkins equation (dotted lines) to extract MO etch rates under these conditions. MgO (a) dissolved within 30 s, ZnO (b) in 1 min, while CoO (c) took 8 h to completely dissolve.

and within MO (Figure S9), rather than proceeding via a gradual dissolution of the solid. This outcome highlights a unique aspect of this chemistry in that the surface area of the MO increases along the reaction trajectory, while the primary dimensions of the particle do not change dramatically at early stages in the reaction. With these phenomena in mind, we were able to fit the disappearing/emerging peaks in the in situ FT-IR using the Prout−Tompkins equation.[54] The physical model from which this equation arises accounts for both the initial acceleratory kinetics due to the increase in reactive surface area (Figure S9) and the deceleratory kinetics, due to the depletion of metal oxide starting material with time. The experimental data points have been thus fitted with the following equation:

$$\log\left(\frac{f}{1-f}\right) = k(t - t_0)$$

where f is the extent of reaction, k is the etching rate constant, and t_0 is the characteristic time of etching. Our treatment of the data in this manner allowed us to extract effective rate constants for MO etching by salicylic acid for MgO, ZnO, and CoO (Table S2).

The modeled time constants indicated that complete etching of the MO under these reaction conditions varied from tens of seconds for ZnO and MgO to hours for CoO. These data were consistent with the relative rates of $M_2(dobpdc)$ formation (fast

for M = Zn and Mg, slower for M = Co), supporting our hypothesis that fast MO etching is critical for optimized $M_2(dobpdc)$ synthesis and that etching is rate-limiting overall.

Minute-MOFs: Ultrafast Synthesis of $M_2(dobpdc)$ from MO Colloidal Nanocrystal Precursors. Based on this insight into the rate-determining step, we offer further a means to push $M_2(dobpdc)$ synthesis to its fringe kinetic limit: substitute commercially available MO powders with custom-prepared divalent MO colloidal NCs. Colloidal nanocrystals, in principle, offer at least an order of magnitude increase in available surface area. Nonetheless, to maximize interfacial contact area between the NCs and the transforming solution of $H_4(dobpdc)$ in DMF, we elected to remove the NC's native coordinating organic ligands using BF_3-mediated chemistry recently developed in our group[39] (Figures S10−S11). Cationic naked nanocrystals[39,55,56] generated in this manner yield homogeneous dispersions in DMF, which may further benefit reaction kinetics; furthermore, use of these dispersions in DMF obviates the use of multiple solvents in the reaction mixture, which is known to influence MOF nucleation, crystal growth, and Ostwald ripening.[57−59] This BF_3-mediated ligand-stripping procedure was carried out on colloidal ZnO and CoO nanocrystals as archetypes for moderate- and slow-etching MO materials (Figure 4), respectively; these were hypothesized to benefit most from any rate acceleration offered by increased surface area and homogeneous reaction conditions.

Indeed, by adding dispersions of naked ZnO NCs (100 mg mL^{-1}) (Figure S10) to $H_4(dobpdc)$ in DMF ($[H_4(dobpdc)]_0 =$ 0.50 M) at 120 °C, an instantaneous reaction was observed. Care was taken to acquire aliquots along the growth trajectory (30 s−1 h). The reaction products obtained from these aliquots were analyzed by SEM and XRD (Figure 5a,b) after being rinsed with DMF and methanol. Notably, MOF signatures ($\theta =$ 6°−9°) in the XRD were evident even after 30 s, and crystalline ZnO was no longer observed ($\theta = 30°−40°$). The corresponding SEM images along the reaction trajectory showed an exceptionally fast evolution in composition within the first 2 min, while the morphology (and crystallinity) of the material did not change significantly after up to 1 h of reaction. Close examination of the SEM series highlights that MOFs grown under these conditions originate from urchin-like structures, which fall apart along the reaction trajectory and ultimately result in well-dispersed crystalline needles (Figure 5b).

The accelerated pace of this MO-to-MOF transformation was likewise observed for naked colloidal CoO NCs (Figure S11),[40] where the analogous transformation from bulk MO precursors was particularly sluggish. As with ZnO, the chemical transformation from naked CoO NCs to $Co_2(dobpdc)$ MOFs was observed over a time-span of 30 s−1 h using our standard conditions. The XRD peaks at 43° and 49°, ascribed to unreacted CoO, were only observed within the first 2 min of reaction. After 2 min, MOF crystals were clearly visible both from XRD and SEM (Figure 5c,d). Furthermore, after 5 min, the CoO is completely etched and $Co_2(dobpdc)$ is prevalent. The morphology of the $Co_2(dobpdc)$ crystals did not change appreciably up to 1 h. Thus, we reason that the slow-etching metal oxides benefit most from the larger available surface area of naked MO NCs as hypothesized. We conclude from our work that colloidal divalent metal oxide nanocrystals[60−64] are unexpected yet privileged precursors to this important family of MOFs and may be so for others. Our work also challenges the
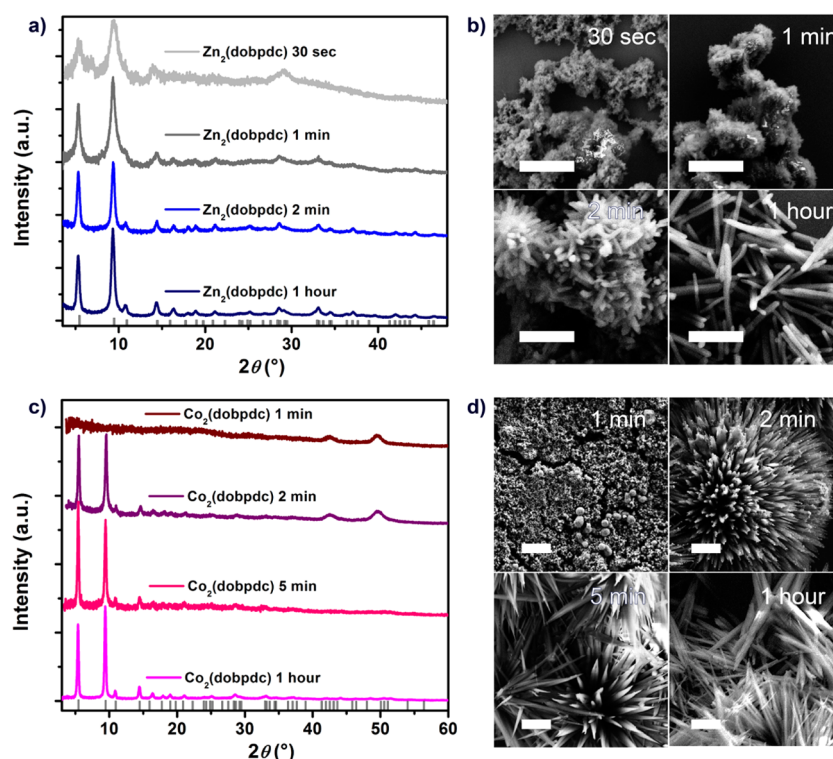
Figure 5. XRD patterns (a) and corresponding SEM images (b) acquired from reaction products along the reaction trajectory from 7 nm colloidal ZnO NCs to $Zn_2(dobpdc)$; and the same (c,d) along the reaction trajectory from 9 nm colloidal CoO NCs to $Co_2(dobpdc)$. Scale bars are (b) 1 μm and (d) 2 μm.

conventional wisdom that the orchestration of events leading to MOF crystallization is time-intensive.[2,34,36,57,58]

CONCLUSIONS

As we continue to translate new MOF discoveries into robust CO_2-capture and other clean energy technologies, the materials requirements to do so demand that we also lay the foundations for expedient and scalable MOF production. Our focus here on the fundamental materials chemistry governing expedient $M_2(dobpdc)$ formation from metal oxide precursors via dissolution−crystallization identified MO etching as rate-limiting. We show that for fast-etching MO materials (e.g., MgO and ZnO), their application as nanopowders is sufficient to reduce reaction times from hours (or days) to minutes. We also demonstrate the fringe kinetic limit of this scheme by employing colloidal MO nanocrystals as $M_2(dobpdc)$ precursors. Here, the interconversion of ZnO to $Zn_2(dobpdc)$ was achieved in less than 1 min using 7 nm ligand-free ZnO nanocrystals. More importantly, however, we found that the kinetic barriers related to MOF formation that arise from slow-etching metal oxides (from commercial powders) can be overcome when the higher surface-area colloidal nanocrystal precursors are used: in the case of CoO, the reaction time was reduced by 2 orders of magnitude, to less than 5 min. Our understanding of the reaction trajectory was informed by both ex situ SEM and in situ FT-IR, which revealed an unexpected metal oxide-to-MOF mechanism that did not proceed via pseudomorphic replication or incur self-limited growth of MOF onto the MO substrate. We also found success in using this procedure to prepare other MOFs, including $M_2(dobdc)$ for M = Co, Ni, Fe, and Zn. While there is still much to be learned from this new reaction scheme at the atomic- and molecular-

scales, our understanding at the nano- to macro- continues to highlight the underexplored opportunities in precursor design and reaction engineering, with minute-MOFs as an important guidepost on that path.

METHODS

Materials. Cobalt oxide (99.998% trace metals basis) was purchased from Alfa Aesar, while magnesium oxide (99% trace metal basis, ~325 mesh), zinc oxide (99.0% (KT)), manganese oxide (99.99% trace metals basis), and nickel oxide (99.99% trace metals basis) were purchased from Sigma-Aldrich. All the other chemicals, reagents, and solvents were purchased from Sigma-Aldrich and used as received without further purification.

Synthesis of 4,4′-Dihydroxy-(1,1′-biphenyl)-3,3′-dicarboxylic Acid ($H_4(dobpdc)$). $H_4(dobpdc)$ was synthesized using a previously reported procedure.[47] Briefly, 4,4′-dihydroxybiphenyl (1.16 g, 6.24 mmol), $KHCO_3$ (2.00 g, 20.0 mmol), solid CO_2 (4.2 g), and 1,2,4-trichlorobenzene (3 mL) were added to a PTFE insert within a 20 mL steel pressure reactor and heated at 255 °C for 17 h. After cooling to room temperature, the mixture was rinsed with diethyl ether and filtered. The collected solid was suspended in distilled water (300 mL) and again filtered. To the filtrate, conc. HCl was added dropwise until pH 2 was reached. The resulting crude product was collected by filtration. The material was recrystallized overnight at 4 °C in 50 mL of acetone and 50 mL of water per gram of crude material. ^{1}H NMR (500 MHz, DMSO-d_6): δ = 14.40−13.90 (br, 2H) 11.20−11.30 (br, 2H), 7.97 (d, 2H, J = 2.4 Hz), 7.80 (dd, 2H, J = 8.6 Hz, J = 2.4 Hz), 7.05 (d, 2H, J = 8.6 Hz).

Synthesis of $M_2(dobpdc)$ (M = Zn, Mg, Mn, Co, Ni) from Commercial MO Powders. A 4 mL dram vial was charged with DMF (0.20 mL) and $H_4(dobpdc)$ (27.4 mg, 0.1 mmol). The vial was heated to 120 °C in a thermally insulating aluminum block allowing for complete dissolution of the ligand, resulting in an initial ligand concentration of $[H_4(dobpdc)]_0$ = 0.50 M. The desired MO powder (0.2 mmol) was then added, and the reaction mixture maintained at 120 °C for a defined reaction time: 10 min for $Mg_2(dobpdc)$, 1 h for

Zn$_2$(dobpdc), 3 h for Co$_2$(dobpdc), 3 h for Mn$_2$(dobpdc), and 20 h for Ni$_2$(dobpdc). After cooling the reaction mixture, an additional portion of DMF was added, and the product isolated after centrifugation of the crude M$_2$(dobpdc) solids. The solids were further washed with DMF (2×) and then methanol (3×). M$_2$(dobpdc) solids were activated under dynamic vacuum (<20 μTorr) at 250 °C for 12 h. Porosimetry measurements were carried out immediately after activation, reducing to a minimum the MOF's exposure to air. Attempts to yield Fe$_2$(dobpdc) and Cu$_2$(dobpdc) from FeO and CuO commercial powders were not immediately successful using these reaction conditions.

Insertion of *N,N*′-Dimethylethylenediamine (mmen) in Mg$_2$(dobpdc). Fully activated Mg$_2$(dobpdc) (30 mg) was immersed in 10 mL of anhydrous hexane containing *N,N*′-dimethylethylenediamine (1 mL). After 4 h, excess mmen-Mg$_2$(dobpdc) was rinsed from the MOFs using fresh hexane, and the MOFs activated under dynamic vacuum at 100 °C for 4 h.

Synthesis of ZnO Nanocrystals. ZnO nanocrystals were synthesized following a previously reported procedure.[39] Briefly, to a 500 mL round-bottom flask, KOH (902 mg, 16 mmol) was dissolved in methanol (150 mL). The solution was heated to 60 °C while stirring and kept at this temperature for 30 min. Next, zinc acetate dihydrate (1.757 g, 8.0 mmol) in methanol (50 mL) was added and the temperature raised to 60 °C. The reaction was allowed to proceed for 2 h before quenching the reaction (i.e., by allowing the vessel to cool to RT). Colloidal ZnO NCs were precipitated by adding hexanes (5 volumetric equivalents) and isopropanol (1 volumetric equivalent). The ZnO solids were isolated by centrifugation. The NCs were redispersed in the minimal volume of methanol, and the above cleaning steps were repeated twice. To interchange the surface hydroxyls to organic surfactants, ZnO NCs were dispersed in chloroform (3 mL) containing oleylamine (375 μL) and oleic acid (121 μL) for 12 h before precipitating ligand-coated ZnO NCs using acetone. Excess ligand was removed from the final product by repeated (3×) precipitation (acetone) and redispersion (hexanes). Full characterization of these ∼7 nm ZnO NCs is given in Figure S10a,e,f.

Synthesis of CoO Nanocrystals. Cobalt oxide nanocrystals were synthesized using a slightly modified procedure reported elsewhere.[40] To a 150 mL 3-neck round-bottom flask was added solid hexadecylamine (HDA) (38.6 g, 160 mmol), which was subsequently melted upon heating at 70 °C. Cobalt acetylacetonate [Co(acac)$_2$] (514 mg, 2 mmol) was then added to the solvent melt, and the reaction mixture degassed at 100 °C for 1 h under dynamic vacuum. To grow the nanocrystals, the reaction temperature was raised to 240 °C and kept at that temperature for 3 h before raising it to 260 °C for an additional 30 min. During heating, the initially pink solution turned purple and dark green; at this stage, the reaction mixture appeared turbid. The reaction mixture was quenched by rapid cooling using an air stream. CoO NCs prepared in this manner were cubic phase (confirmed by XRD, see Figure S11c) with a size of ∼9 nm (Figure S11d,e).

Preparation of Naked MO Colloidal Nanocrystals. Nanocrystals were relieved of their coordinating organic ligands following a procedure previously developed by us.[39] Briefly, in a nitrogen glovebox, a dispersion of MO nanocrystals in hexanes (1 mL) was introduced to a glass vial containing DMF (1 mL) and BF$_3$:Et$_2$O (100 μL, 36% w/w in Et$_2$O) and toluene (7 mL). The ligand-stripped nanocrystals precipitated over a few min and were subsequently isolated by centrifugation and decanting (discarding) the supernatant. Further purification was carried out by several cycles of redispersion in DMF (1 mL), precipitation upon addition of hexanes/toluene (1:7, 8 mL), centrifugation (5 min), and decanting off the supernatant. Purified samples of naked NCs were dispersed in DMF to obtain a final concentration of 100 μmol mL^{-1}.

Synthesis of Zn$_2$(dobpdc) or Co$_2$(dobpdc) from Ligand-Stripped ZnO or CoO NCs. H$_4$(dobpdc) (27.4 mg, 100 μmol) in DMF (100 μL) was heated to 120 °C before adding naked ZnO or CoO NCs as a dispersion in DMF (100 μL, 100 μmol mL^{-1}). Aliquots were taken at 30 s, 1 min, 2 min, 5 min, 10 min, 30 min, and 1 h.

Zn$_2$(dobpdc) or Co$_2$(dobpdc) thus produced were washed with DMF and methanol as described above prior to analysis.

Brunauer−Emmett−Teller (BET) Surface Area Measurements. Dry, freshly activated MOF samples were transferred to a preweighed glass sample tube under nitrogen atmosphere. In a typical experiment, 40 mg of adsorbent were loaded into a Micromeritics TriStar II, put under vacuum (<10 mTorr) and cooled to 77 K. The adsorption measurement was performed using N$_2$.

CO$_2$ Adsorption Measurements. mmen-Mg$_2$(dobpdc) was activated and transferred to a Micrometric ASAP 2020 instrument. Pressure range for CO$_2$ introduced was 0−1 bar.

SEM. Images were obtained with a Zeiss Gemini Ultra-55 analytical scanning electron microscope equipped with secondary electron detectors at beam energy of 3 keV. Samples were deposited onto silicon wafers from a dispersion of M$_2$(dobpdc) in methanol; loaded substrates were dried in air prior to imaging.

XRD. Spectra were recorded in air on a Bruker Gadds-8 diffractometer with Cu−Kα source operating at 40 kV and 20 mA.

■ ASSOCIATED CONTENT

Ⓢ Supporting Information

The Supporting Information is available free of charge on the ACS Publications website at DOI: 10.1021/acs.chemmater.6b00494.

Figures S1−S11 and Tables S1 and S2 (PDF)

■ AUTHOR INFORMATION

Corresponding Author

*E-mail: bahelms@lbl.gov.

Notes

The authors declare no competing financial interest.

■ ACKNOWLEDGMENTS

■ ABBREVIATIONS

M$_2$(dobpdc), metal 4,4′-dioxido-3,3′-biphenyldicarboxylate metal−organic frameworks; M$_2$(dobdc), metal 2,5-dioxido-1,4-benzenedicarboxylate metal−organic frameworks

■ REFERENCES

(1) Davis, M. E. Ordered Porous Materials for Emerging Applications. *Nature* **2002**, *417*, 813−821.

(2) Yaghi, O. M.; O'Keeffe, M.; Ockwig, N. W.; Chae, H. K.; Eddaoudi, M.; Kim, J. Reticular Synthesis and the Design of New Materials. *Nature* **2003**, *423*, 705−714.

(3) Horcajada, P.; Gref, R.; Baati, T.; Allan, P. K.; Maurin, G.; Couvreur, P.; Férey, G.; Morris, R. E.; Serre, C. Metal−Organic Frameworks in Biomedicine. *Chem. Rev.* **2012**, *112*, 1232−1268.

(4) Horcajada, P.; Chalati, T.; Serre, C.; Gillet, B.; Sebrie, C.; Baati, T.; Eubank, J. F.; Heurtaux, D.; Clayette, P.; Kreuz, C.; et al. Porous

Metal-Organic-Framework Nanoscale Carriers as a Potential Platform for Drug Delivery and Imaging. *Nat. Mater.* **2010**, *9*, 172−178.

(5) Fujita, M.; Kwon, Y. J.; Washizu, S.; Ogura, K. Preparation, Clathration Ability, and Catalysis of a Two-Dimensional Square Network Material Composed of Cadmium(II) and 4,4′-Bipyridine. *J. Am. Chem. Soc.* **1994**, *116*, 1151−1152.

(6) Lee, J.; Farha, O. K.; Roberts, J.; Scheidt, K. A.; Nguyen, S. T.; Hupp, J. T. Metal-Organic Framework Materials as Catalysts. *Chem. Soc. Rev.* **2009**, *38*, 1450−1459.

(7) Liu, J.; Chen, L.; Cui, H.; Zhang, J.; Zhang, L.; Su, C.-Y. Applications of Metal-Organic Frameworks in Heterogeneous Supra-molecular Catalysis. *Chem. Soc. Rev.* **2014**, *43*, 6011−6061.

(8) Kreno, L. E.; Leong, K.; Farha, O. K.; Allendorf, M.; Van Duyne, R. P.; Hupp, J. T. Metal−Organic Framework Materials as Chemical Sensors. *Chem. Rev.* **2012**, *112*, 1105−1125.

(9) Cui, Y.; Yue, Y.; Qian, G.; Chen, B. Luminescent Functional Metal−Organic Frameworks. *Chem. Rev.* **2012**, *112*, 1126−1162.

(10) Campbell, M. G.; Sheberla, D.; Liu, S. F.; Swager, T. M.; Dincă, M. Cu_3(hexaiminotriphenylene)$_2$: An Electrically Conductive 2D Metal−Organic Framework for Chemiresistive Sensing. *Angew. Chem., Int. Ed.* **2015**, *54*, 4349−4352.

(11) Kobayashi, Y.; Jacobs, B.; Allendorf, M. D.; Long, J. R. Conductivity, Doping, and Redox Chemistry of a Microporous Dithiolene-Based Metal−Organic Framework. *Chem. Mater.* **2010**, *22*, 4120−4122.

(12) Silva, C. G.; Corma, A.; Garcia, H. Metal-Organic Frameworks as Semiconductors. *J. Mater. Chem.* **2010**, *20*, 3141−3156.

(13) Shekhah, O.; Liu, J.; Fischer, R. A.; Wöll, C. MOF Thin Films: Existing and Future Applications. *Chem. Soc. Rev.* **2011**, *40*, 1081−1106.

(14) Sheberla, D.; Sun, L.; Blood-Forsythe, M. A.; Er, S.; Wade, C. R.; Brozek, C. K.; Aspuru-Guzik, A.; Dincă, M. High Electrical Conductivity in Ni_3(2,3,6,7,10,11-hexaiminotriphenylene)$_2$, a Semi-conducting Metal−Organic Graphene Analogue. *J. Am. Chem. Soc.* **2014**, *136*, 8859−8862.

(15) Stavila, V.; Talin, A. A.; Allendorf, M. D. MOF-Based Electronic and Opto-Electronic Devices. *Chem. Soc. Rev.* **2014**, *43*, 5994−6010.

(16) Talin, A. A.; Centrone, A.; Ford, A. C.; Foster, M. E.; Stavila, V.; Haney, P.; Kinney, R. A.; Szalai, V.; El Gabaly, F.; Yoon, H. P.; et al. Tunable Electrical Conductivity in Metal-Organic Framework Thin-Film Devices. *Science* **2014**, *343*, 66−69.

(17) Park, S. S.; Hontz, E. R.; Sun, L.; Hendon, C. H.; Walsh, A.; Van Voorhis, T.; Dincă, M. Cation-Dependent Intrinsic Electrical Conductivity in Isostructural Tetrathiafulvalene-Based Microporous Metal−Organic Frameworks. *J. Am. Chem. Soc.* **2015**, *137*, 1774−1777.

(18) Wiers, B. M.; Foo, M.-L.; Balsara, N. P.; Long, J. R. A Solid Lithium Electrolyte via Addition of Lithium Isopropoxide to a Metal−Organic Framework with Open Metal Sites. *J. Am. Chem. Soc.* **2011**, *133*, 14522−14525.

(19) Morozan, A.; Jaouen, F. Metal−Organic Frameworks for Electrochemical Applications. *Energy Environ. Sci.* **2012**, *5*, 9269−9290.

(20) Horike, S.; Umeyama, D.; Kitagawa, S. Ion Conductivity and Transport by Porous Coordination Polymers and Metal−Organic Frameworks. *Acc. Chem. Res.* **2013**, *46*, 2376−2384.

(21) Zhang, Z.; Yoshikawa, H.; Awaga, K. Monitoring the Solid-State Electrochemistry of Cu(2,7-AQDC) (AQDC = Anthraquinone Dicarboxylate) in a Lithium Battery: Coexistence of Metal and Ligand Redox Activities in a Metal−Organic Framework. *J. Am. Chem. Soc.* **2014**, *136*, 16112−16115.

(22) Aubrey, M. L.; Ameloot, R.; Wiers, B. M.; Long, J. R. Metal-Organic Frameworks as Solid Magnesium Electrolytes. *Energy Environ. Sci.* **2014**, *7*, 667−671.

(23) Li, J.-R.; Kuppler, R. J.; Zhou, H.-C. Selective Gas Adsorption and Separation in Metal-Organic Frameworks. *Chem. Soc. Rev.* **2009**, *38*, 1477−1504.

(24) Bae, T.-H.; Lee, J. S.; Qiu, W.; Koros, W. J.; Jones, C. W.; Nair, S. A High-Performance Gas-Separation Membrane Containing Submicrometer-Sized Metal−Organic Framework Crystals. *Angew. Chem., Int. Ed.* **2010**, *49*, 9863−9866.

(25) Zhang, C.; Lively, R. P.; Zhang, K.; Johnson, J. R.; Karvan, O.; Koros, W. J. Unexpected Molecular Sieving Properties of Zeolitic Imidazolate Framework-8. *J. Phys. Chem. Lett.* **2012**, *3*, 2130−2134.

(26) Brown, A. J.; Johnson, J. R.; Lydon, M. E.; Koros, W. J.; Jones, C. W.; Nair, S. Continuous Polycrystalline Zeolitic Imidazolate Framework-90 Membranes on Polymeric Hollow Fibers. *Angew. Chem., Int. Ed.* **2012**, *51*, 10615−10618.

(27) Sumida, K.; Rogow, D. L.; Mason, J. A.; McDonald, T. M.; Bloch, E. D.; Herm, Z. R.; Bae, T.-H.; Long, J. R. Carbon Dioxide Capture in Metal−Organic Frameworks. *Chem. Rev.* **2012**, *112*, 724−781.

(28) Bloch, E. D.; Queen, W. L.; Krishna, R.; Zadrozny, J. M.; Brown, C. M.; Long, J. R. Hydrocarbon Separations in a Metal-Organic Framework with Open Iron(II) Coordination Sites. *Science* **2012**, *335*, 1606−1610.

(29) Zhang, K.; Lively, R. P.; Zhang, C.; Chance, R. R.; Koros, W. J.; Sholl, D. S.; Nair, S. Exploring the Framework Hydrophobicity and Flexibility of ZIF-8: From Biofuel Recovery to Hydrocarbon Separations. *J. Phys. Chem. Lett.* **2013**, *4*, 3618−3622.

(30) Brown, A. J.; Brunelli, N. A.; Eum, K.; Rashidi, F.; Johnson, J. R.; Koros, W. J.; Jones, C. W.; Nair, S. Interfacial Microfluidic Processing of Metal-Organic Framework Hollow Fiber Membranes. *Science* **2014**, *345*, 72−75.

(31) Eddaoudi, M.; Kim, J.; Rosi, N.; Vodak, D.; Wachter, J.; O'Keeffe, M.; Yaghi, O. M. Systematic Design of Pore Size and Functionality in Isoreticular MOFs and Their Application in Methane Storage. *Science* **2002**, *295*, 469−472.

(32) Rosi, N. L.; Eckert, J.; Eddaoudi, M.; Vodak, D. T.; Kim, J.; O'Keeffe, M.; Yaghi, O. M. Hydrogen Storage in Microporous Metal-Organic Frameworks. *Science* **2003**, *300*, 1127−1129.

(33) Millward, A. R.; Yaghi, O. M. Metal−Organic Frameworks with Exceptionally High Capacity for Storage of Carbon Dioxide at Room Temperature. *J. Am. Chem. Soc.* **2005**, *127*, 17998−17999.

(34) Shekhah, O.; Wang, H.; Zacher, D.; Fischer, R. A.; Wöll, C. Growth Mechanism of Metal−Organic Frameworks: Insights into the Nucleation by Employing a Step-by-Step Route. *Angew. Chem., Int. Ed.* **2009**, *48*, 5038−5041.

(35) Goesten, M. G.; Stavitski, E.; Juan-Alcañiz, J.; Martiñez-Joaristi, A.; Petukhov, A. V.; Kapteijn, F.; Gascon, J. Small-Angle X-Ray Scattering Documents the Growth of Metal-Organic Frameworks. *Catal. Today* **2013**, *205*, 120−127.

(36) Férey, G.; Haouas, M.; Loiseau, T.; Taulelle, F. Nanoporous Solids: How Do They Form? An In Situ Approach. *Chem. Mater.* **2014**, *26*, 299−309.

(37) Patterson, J. P.; Abellan, P.; Denny, M. S.; Park, C.; Browning, N. D.; Cohen, S. M.; Evans, J. E.; Gianneschi, N. C. Observing the Growth of Metal−Organic Frameworks by in Situ Liquid Cell Transmission Electron Microscopy. *J. Am. Chem. Soc.* **2015**, *137*, 7322−7328.

(38) Chalati, T.; Horcajada, P.; Gref, R.; Couvreur, P.; Serre, C. Optimisation of the Synthesis of MOF Nanoparticles Made of Flexible Porous Iron Fumarate MIL-88A. *J. Mater. Chem.* **2011**, *21*, 2220−2227.

(39) Doris, S. E.; Lynch, J. J.; Li, C. Y.; Wills, A. W.; Urban, J. J.; Helms, B. A. Mechanistic Insight into the Formation of Cationic Naked Nanocrystals Generated under Equilibrium Control. *J. Am. Chem. Soc.* **2014**, *136*, 15702−15710.

(40) Li, Y.; Afzaal, M.; O'Brien, P. The Synthesis of Amine-Capped Magnetic (Fe, Mn, Co, Ni) Oxide Nanocrystals and Their Surface Modification for Aqueous Dispersibility. *J. Mater. Chem.* **2006**, *16*, 2175−2180.

(41) Friscic, T.; Fabian, L. Mechanochemical Conversion of a Metal Oxide into Coordination Polymers and Porous Frameworks Using Liquid-Assisted Grinding (LAG). *CrystEngComm* **2009**, *11*, 743−745.

(42) Yue, Y.; Mehio, N.; Binder, A. J.; Dai, S. Synthesis of Metal-Organic Framework Particles and Thin Films via Nanoscopic Metal Oxide Precursors. *CrystEngComm* **2015**, *17*, 1728−1735.

(43) Reboul, J.; Furukawa, S.; Horike, N.; Tsotsalas, M.; Hirai, K.; Uehara, H.; Kondo, M.; Louvain, N.; Sakata, O.; Kitagawa, S.

Mesoscopic Architectures of Porous Coordination Polymers Fabricated by Pseudomorphic Replication. *Nat. Mater.* **2012**, *11*, 717−723.

(44) Zanchetta, E.; Malfatti, L.; Ricco, R.; Styles, M. J.; Lisi, F.; Coghlan, C. J.; Doonan, C. J.; Hill, A. J.; Brusatin, G.; Falcaro, P. ZnO as an Efficient Nucleating Agent for Rapid, Room Temperature Synthesis and Patterning of Zn-Based Metal−Organic Frameworks. *Chem. Mater.* **2015**, *27*, 690−699.

(45) Stassen, I.; Campagnol, N.; Fransaer, J.; Vereecken, P.; De Vos, D.; Ameloot, R. Solvent-Free Synthesis of Supported ZIF-8 Films and Patterns through Transformation of Deposited Zinc Oxide Precursors. *CrystEngComm* **2013**, *15*, 9308−9311.

(46) Zhan, W.; Kuang, Q.; Zhou, J.; Kong, X.; Xie, Z.; Zheng, L. Semiconductor@Metal−Organic Framework Core−Shell Heterostructures: A Case of ZnO@ZIF-8 Nanorods with Selective Photoelectrochemical Response. *J. Am. Chem. Soc.* **2013**, *135*, 1926−1933.

(47) McDonald, T. M.; Lee, W. R.; Mason, J. A.; Wiers, B. M.; Hong, C. S.; Long, J. R. Capture of Carbon Dioxide from Air and Flue Gas in the Alkylamine-Appended Metal-Organic Framework Mmen-Mg2-(dobpdc). *J. Am. Chem. Soc.* **2012**, *134*, 7056−7065.

(48) McDonald, T. M.; Mason, J. A.; Kong, X.; Bloch, E. D.; Gygi, D.; Dani, A.; Crocella, V.; Giordanino, F.; Odoh, S. O.; Drisdell, W. S.; et al. Cooperative Insertion of CO_2 in Diamine-Appended Metal-Organic Frameworks. *Nature* **2015**, *519*, 303−308.

(49) Lee, W. R.; Jo, H.; Yang, L.-M.; Lee, H.; Ryu, D. W.; Lim, K. S.; Song, J. H.; Min, D. Y.; Han, S. S.; Seo, J. G.; et al. Exceptional CO_2 Working Capacity in a Heterodiamine-Grafted Metal−organic Framework. *Chem. Sci.* **2015**, *6*, 3697−3705.

(50) Wu, D.; McDonald, T. M.; Quan, Z.; Ushakov, S. V.; Zhang, P.; Long, J. R.; Navrotsky, A. Thermodynamic Complexity of Carbon Capture in Alkylamine-Functionalized Metal-Organic Frameworks. *J. Mater. Chem. A* **2015**, *3*, 4248−4254.

(51) Drisdell, W. S.; Poloni, R.; McDonald, T. M.; Pascal, T. A.; Wan, L. F.; Pemmaraju, C. D.; Vlaisavljevich, B.; Odoh, S. O.; Neaton, J. B.; Long, J. R.; et al. Probing the Mechanism of CO_2 Capture in Diamine-Appended Metal-Organic Frameworks Using Measured and Simulated X-Ray Spectroscopy. *Phys. Chem. Chem. Phys.* **2015**, *17*, 21448−21457.

(52) Vlaisavljevich, B.; Odoh, S. O.; Schnell, S. K.; Dzubak, A. L.; Lee, K.; Planas, N.; Neaton, J. B.; Gagliardi, L.; Smit, B. CO_2 Induced Phase Transitions in Diamine-Appended Metal-Organic Frameworks. *Chem. Sci.* **2015**, *6*, 5177−5185.

(53) Rochelle, G. T. Amine Scrubbing for CO_2 Capture. *Science* **2009**, *325*, 1652−1654.

(54) Prout, E. G.; Tompkins, F. C. The Thermal Decomposition of Potassium Permanganate. *Trans. Faraday Soc.* **1944**, *40*, 488−498.

(55) Dong, A.; Ye, X.; Chen, J.; Kang, Y.; Gordon, T.; Kikkawa, J. M.; Murray, C. B. *J. Am. Chem. Soc.* **2011**, *133*, 998−1006.

(56) Rosen, E. L.; Buonsanti, R.; Llordes, A.; Sawvel, A. M.; Milliron, D. J.; Helms, B. A. Exceptionally Mild Reactive Stripping of Native Ligands from Nanocrystal Surfaces by Using Meerwein's Salt. *Angew. Chem., Int. Ed.* **2012**, *51*, 684−689.

(57) Lin, W.; Rieter, J. W.; Taylor, K. M. L. Modular Synthesis of Functional Nanoscale Coordination Polymers. *Angew. Chem., Int. Ed.* **2009**, *48*, 650−658.

(58) Spokoyny, A. M.; Kim, D.; Sumrein, A.; Mirkin, C. A. Infinite Coordination Polymer Nano- and Microparticle Structures. *Chem. Soc. Rev.* **2009**, *38*, 1218−1227.

(59) Meckler, S. M.; Li, C.; Queen, W. L.; Williams, T. E.; Long, J. R.; Buonsanti, R.; Milliron, D. J.; Helms, B. A. Sub-Micron Polymer-Zeolitic Imidazolate Framework Layered Hybrids via Controlled Chemical Transformation of Naked ZnO Nanocrystal Films. *Chem. Mater.* **2015**, *27*, 7673−7679.

(60) Chen, Y.; Johnson, E.; Peng, X. Formation of Monodisperse and Shape-Controlled MnO Nanocrystals in Non-Injection Synthesis: Self-Focusing via Ripening. *J. Am. Chem. Soc.* **2007**, *129*, 10937−10947.

(61) Schladt, T. D.; Graf, T.; Tremel, W. Synthesis and Characterization of Monodisperse Manganese Oxide Nanoparticles−Evaluation of the Nucleation and Growth Mechanism. *Chem. Mater.* **2009**, *21*, 3183−3190.

(62) Ning, J.; Xiao, G.; Wang, L.; Zou, B.; Liu, B.; Zou, G. Facile Synthesis of Magnetic Metal (Mn, Fe, Co, and Ni) Oxides Nanocrystals via a Cation-Exchange Reaction. *Nanoscale* **2011**, *3*, 741−745.

(63) Buck, M. R.; Biacchi, A. J.; Schaak, R. E. Insights into the Thermal Decomposition of Co(II) Oleate for the Shape-Controlled Synthesis of Wurtzite-Type CoO Nanocrystals. *Chem. Mater.* **2014**, *26*, 1492−1499.

(64) Fominykh, K.; Feckl, J. M.; Sicklinger, J.; Döblinger, M.; Böcklein, S.; Ziegler, J.; Peter, L.; Rathousky, J.; Scheidt, E.-W.; Bein, T.; et al. Ultrasmall Dispersible Crystalline Nickel Oxide Nanoparticles as High-Performance Catalysts for Electrochemical Water Splitting. *Adv. Funct. Mater.* **2014**, *24*, 3123−3129.